JACS
JOURNAL OF THE AMERICAN CHEMICAL SOCIETY

pubs.acs.org/JACS Article

# Accelerating $CO_2$ Electroreduction to Multicarbon Products via Synergistic Electric−Thermal Field on Copper Nanoneedles

Baopeng Yang,[#] Kang Liu,[#] HuangJingWei Li,[#] Changxu Liu,[#] Junwei Fu, Hongmei Li, Jianan Erick Huang, Pengfei Ou, Tartela Alkayyali, Chao Cai, Yuxia Duan, Hui Liu, Pengda An, Ning Zhang, Wenzhang Li, Xiaoqing Qiu, Chuankun Jia, Junhua Hu, Liyuan Chai, Zhang Lin, Yongli Gao, Masahiro Miyauchi, Emiliano Cortés, Stefan A. Maier,* and Min Liu*

Cite This: J. Am. Chem. Soc. 2022, 144, 3039−3049 Read Online

ACCESS | Metrics & More | Article Recommendations | Supporting Information

**ABSTRACT:** Electrochemical $CO_2$ reduction is a promising way to mitigate $CO_2$ emissions and close the anthropogenic carbon cycle. Among products from $CO_2RR$, multicarbon chemicals, such as ethylene and ethanol with high energy density, are more valuable. However, the selectivity and reaction rate of $C_2$ production are unsatisfactory due to the sluggish thermodynamics and kinetics of C−C coupling. The electric field and thermal field have been studied and utilized to promote catalytic reactions, as they can regulate the thermodynamic and kinetic barriers of reactions. Either raising the potential or heating the electrolyte can enhance C−C coupling, but these come at the cost of increasing side reactions, such as the hydrogen evolution reaction. Here, we present a generic strategy to enhance the local electric field and temperature simultaneously and dramatically improve the electric−thermal synergy desired in electrocatalysis. A conformal coating of ∼5 nm of polytetrafluoroethylene significantly improves the catalytic ability of copper nanoneedles (∼7-fold electric field and ∼40 K temperature enhancement at the tips compared with bare copper nanoneedles experimentally), resulting in an improved $C_2$ Faradaic efficiency of over 86% at a partial current density of more than 250 mA $cm^{-2}$ and a record-high $C_2$ turnover frequency of 11.5 ± 0.3 $s^{-1}$ Cu $site^{-1}$. Combined with its low cost and scalability, the electric−thermal strategy for a state-of-the-art catalyst not only offers new insight into improving activity and selectivity of value-added $C_2$ products as we demonstrated but also inspires advances in efficiency and/or selectivity of other valuable electro-/photocatalysis such as hydrogen evolution, nitrogen reduction, and hydrogen peroxide electrosynthesis.

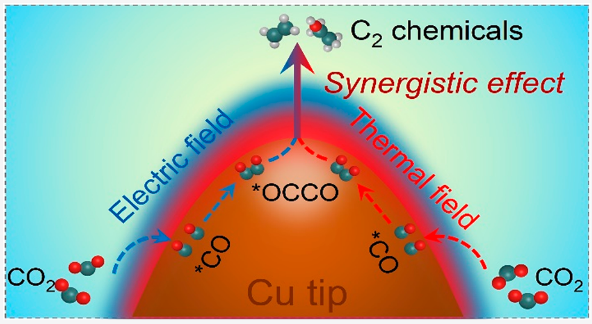


## ■ INTRODUCTION

Electrochemical conversion of carbon dioxide ($CO_2$) into value-added carbon-based feedstocks and fuels by utilizing renewable electricity is a promising technology to mitigate $CO_2$ emissions, fulfill the anthropogenic carbon cycle, and store the excess renewable electricity as chemical energy.[1−3] Among various products produced from the $CO_2$ reduction reaction ($CO_2RR$), two-carbon ($C_2$) hydrocarbons and oxygenates, such as ethylene ($C_2H_4$) and ethanol (EtOH), are attractive in view of their high energy densities and major roles in the chemical industry.[1,2] However, the selectivity and reaction rate for $C_2$ productions are still below the demands for practical applications, due to the sluggish thermodynamics and kinetics of C−C coupling.[4−8]

Raising the coverage of *CO, a key intermediate for C−C coupling,[4,5,8] and simultaneously lowering the energy barrier of *CO dimerization on the catalyst would effectively improve C−C coupling.[9−19] Although many efforts have been tried to implement these by regulating the electronic properties of Cu, such as element doping,[9−11] facet control,[12,13] heterojunction interface construction,[14−16] and defect creation,[17−19] the complexity and finiteness of electronic structure tuning impede their applications at scale.

The electric field has been extensively studied and utilized to improve the activity and selectivity of catalytic reactions, as it can accumulate reactants and regulate the thermodynamic barriers of reactions.[20−27] Similar to the electric field, the thermal field can promote the reaction rate through facilitating the kinetic process.[28−32] Therefore, introducing an electric field and thermal field (denoted as electric−thermal field) synchronously on the Cu surface would be an effective way to improve the selectivity and reaction rate of $C_2$ products during $CO_2RR$. A simple way to enhance the electric−thermal field is directly

**Received:** October 24, 2021
**Published:** February 3, 2022

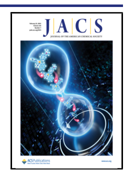






https://doi.org/10.1021/jacs.1c11253
J. Am. Chem. Soc. 2022, 144, 3039−3049

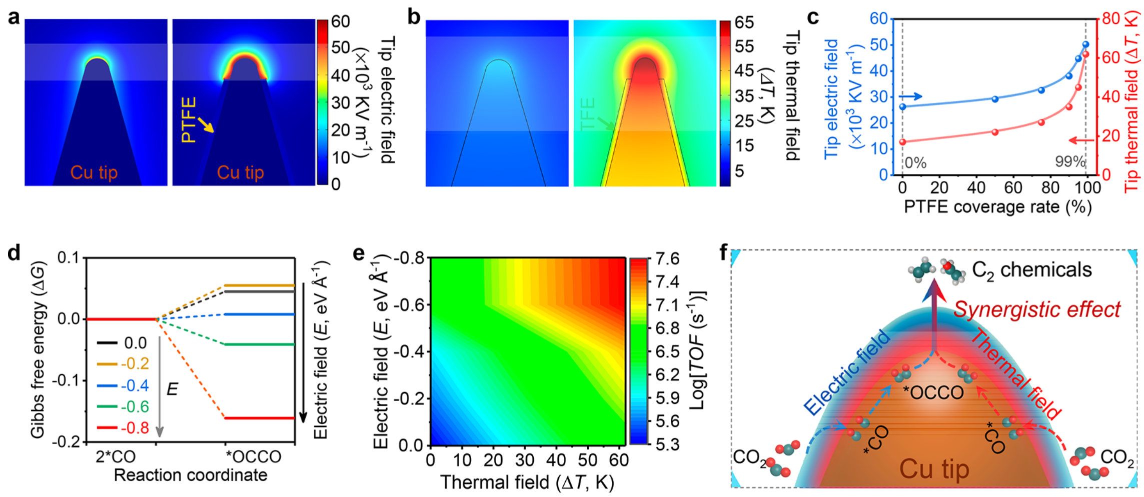


**Figure 1.** FEM simulations and DFT calculations. (a) The electric field distribution on a pristine Cu NN (left) and a Cu NN with 99% PTFE coverage (right). (b) Thermal field distribution on a pristine Cu NN (left) and a Cu NN with 99% PTFE coverage (right). The thermal field ($\Delta T$, K) is the temperature enhancement versus room temperature (298 K). (c) Electric field and thermal field at the Cu NN tips as a function of PTFE coverage rates. (d) Reaction Gibbs free energy diagrams of *CO dimerization to form *OCCO on the Cu(100) surface under different electric fields. (e) TOF map of *CO dimerization on Cu(100) under various electric fields and thermal fields. (f) Schematic illustration of the synergetic effect of tip-induced electric field and thermal field on promoting $C_2$ formation.

raising the applied potential and heating the electrolyte. However, it comes at the cost of increasing the hydrogen evolution reaction (HER) and the generation of $C_1$, because the HER and $C_1$ production are more likely to be activated than $C_2$ production.[20,25,31,33]

In this work, we report a synergetic electric−thermal field strategy, by conformally coating Cu nanoneedle (Cu NN) bodies with polytetrafluoroethylene (PTFE) to produce a locally enhanced local electric−thermal field at the tips, to raise *CO intermediates and facilitate C−C coupling for high-efficiency conversion of $CO_2$ to $C_2$ products. Finite element method (FEM) simulations show that the Cu NN tip possesses a local electric−thermal field, and this electric−thermal field can be further enhanced by pushing electrons to the top tip through covering the Cu NN body with a dielectric polymer. Density functional theory (DFT) calculations indicate the enhanced electric field lowers the Gibbs free energy ($\Delta G$) of C−C coupling, and the enhanced thermal field boosts the reaction rate of C−C coupling. Inspired by these aspects, we synthesize a series of Cu NNs with different PTFE coverage (Cu-PTFE NNs) and verify the electric−thermal field at the tips through the adsorbed $K^+$ concentration and infrared thermal imaging tests, which show about 3-fold enhancement with the increase of PTFE coverage. *In situ* Fourier transform infrared (FTIR) investigations confirm the *CO accumulation and C−C coupling acceleration. As a result, we implement a conversion of $CO_2$ to $C_2$ with a Faradaic efficiency (FE) of over 86%, a half-cell cathodic energy efficiency (CEE) of ∼50% at a partial current density of over 250 mA $cm^{-2}$, and a record-high turnover frequency (TOF) of 11.5 ± 0.3 $s^{-1}$ Cu $site^{-1}$ to the best of our knowledge. This work opens a new avenue to improve the selectivity and activity of Cu-based catalysts. More importantly, the conformal coating may be transferred to other catalytic platforms demanding a synergic effect of improved electric field and temperature at the nanoscale.

## ■ RESULTS AND DISCUSSION

**FEM Simulations and DFT Calculations.** High-curvature metallic structures are known to accumulate electrons and spontaneously increase local electron density and collision, leading to a locally enhanced electric field and high temperature (thermal field) at the tip (Figure S1a).[20,23,34−37] We speculate that the tip-induced electric field and thermal field (defined as the electric−thermal field) can be further enhanced by covering the needle body with a dielectric polymer to concentrate electrons on the very top point of a tip (Figure S1b). To verify this assumption, we employed FEM simulations to investigate the distribution of electron density, electric field, and thermal field on the tip of the Cu NN with different PTFE coverage rates. We found that with the PTFE coverage rates increasing from 0% to 99%, the tip-concentrated electron density showed a 2-fold enhancement (Figures S2 and S3), resulting in an obviously enhanced electric field and thermal field at the tips (Figure 1a,b and Figures S4 and S5). Remarkably, the tip-induced electric field and thermal field showed a sharp enhancement as the PTFE coverage increased and achieved about 2-fold (from 26.3 × $10^3$ to 50.3 × $10^3$ kV $m^{-1}$) and 3-fold (from 17 to 62 K) enhancement, respectively (Figure 1c and Table S1). In contrast to a sharp-tip Cu NN, the electric field and thermal field enhancements are negligible for a quasi-planar Cu nanoparticle (Cu NP) (Figures S6 and S7 and Table S1). We also investigated the relationship between the electric−thermal field and applied bias (Figure S8); the results showed that the tip-induced electric field and thermal field showed an enhancement as applied bias increased.

To explore how the tip-induced electric−thermal field influences the $C_2$ formation, DFT calculations were applied to survey the *CO dimerization process on the Cu surface, which is the key rate-limiting step along the $CO_2$-to-$C_2$ pathway.[38,39] We introduced various electric fields onto the Cu(100) surface, a facet that has been confirmed to favor $C_2$ formation,[40−42] and used an explicit water model[43] to calculate the thermodynamic energy barriers for *CO dimerization (Figure 1d and Table S2). We found that the $\Delta G$ of *CO dimerization decreased with the electric field increasing, suggesting that the electric field is thermodynamically favorable for $C_2$ formation. In order to study the kinetics process of *CO dimerization, we then calculated the activation energy ($\Delta E_a$) and TOF of *CO dimerization via[44]



https://doi.org/10.1021/jacs.1c11253
J. Am. Chem. Soc. 2022, 144, 3039−3049

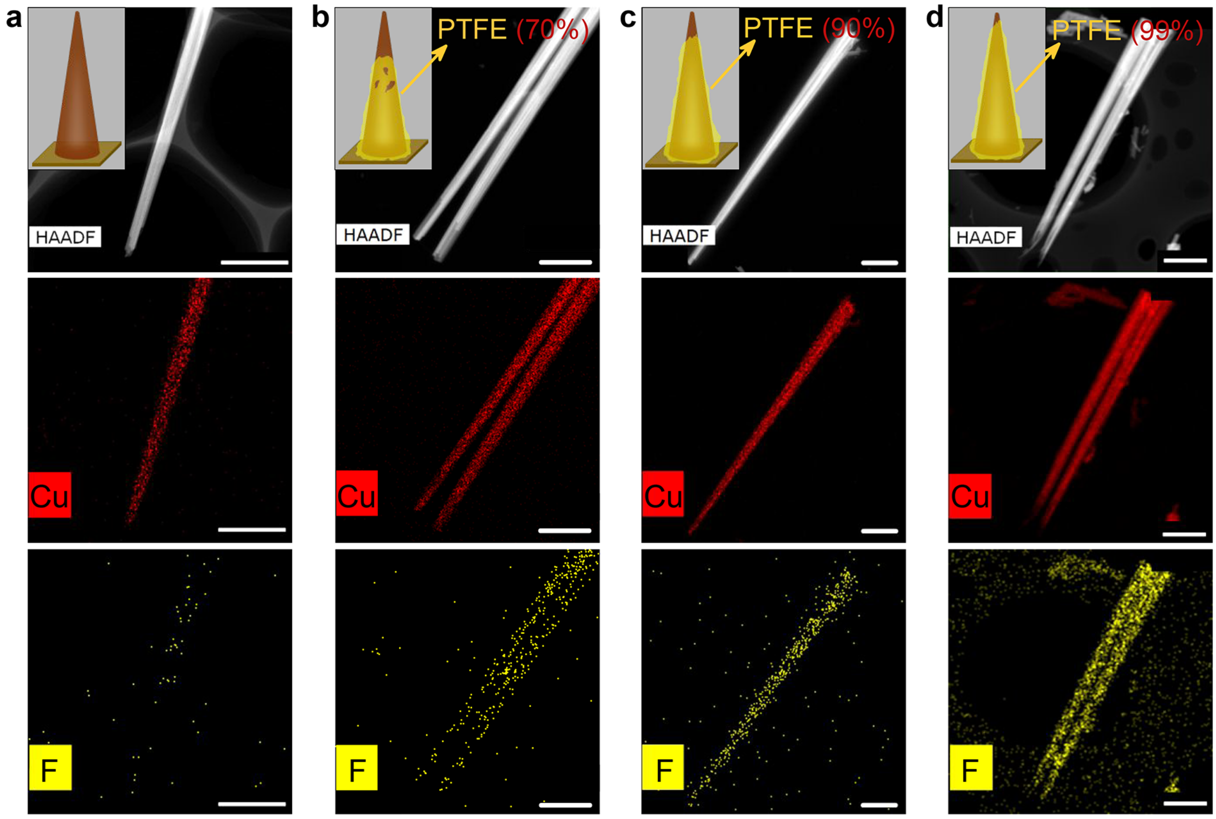


**Figure 2.** Structural characterization. (a−d) HAADF-STEM images and the corresponding elemental mapping of Cu (red) and F (yellow) taken from a section of (a) pristine Cu NN, (b) Cu NN with a PTFE coverage rate of 70% (Cu-PTFE-70 NN), (c) Cu NN with a PTFE coverage rate of 90% (Cu-PTFE-90 NN), and (d) Cu NN with a PTFE coverage rate of 99% (Cu-PTFE-99 NN). Scale bars, 1 $\mu$m. Insets: Schematic illustrations of the coverage status of PTFE on Cu NN bodies. PTFE coverage rates were estimated from SEM and TEM analyses.

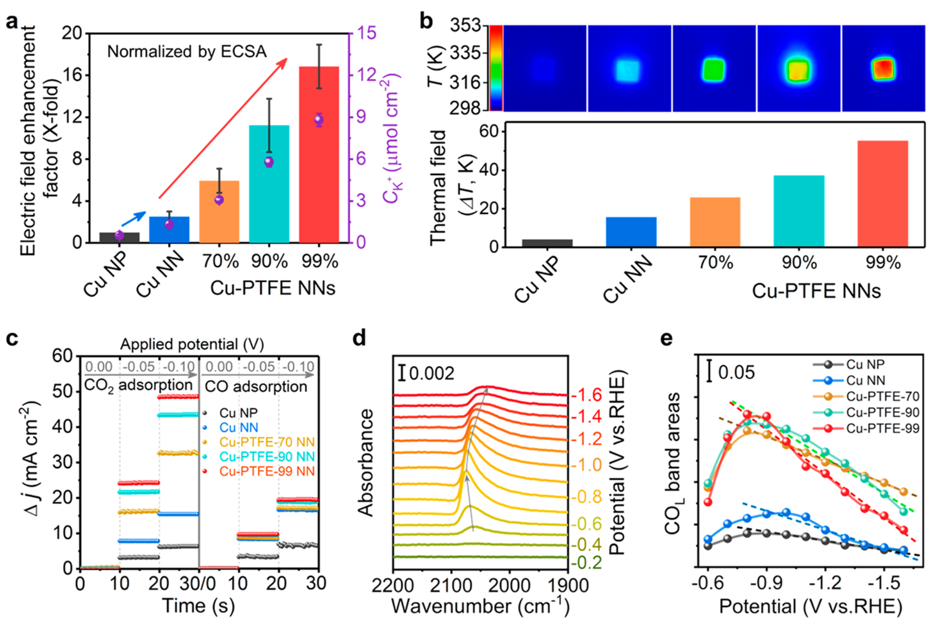


**Figure 3.** Electric−thermal field detection and enhancement mechanism investigation. (a) Electric field enhancement factor and the concentration of adsorbed $K^+$ ions on the surface of electrodes at a potential of −1.5 V vs RHE, normalized by ECSA. Error bars correspond to the standard deviation of three independent electrode measurements. The electric field enhancement factor was estimated from the adsorbed $K^+$ concentrations by using a Cu NP as reference. (b) Infrared thermal imaging of the electrodes (top) and corresponding thermal field magnitude (bottom) at an applied constant current. (c) Results of $CO_2$ (left) and CO (right) adsorption responses under different applied voltages. (d) *In situ* ATR-FTIR spectra of a Cu-PTFE-99 NN electrode under different potentials. (e) Stretching band areas of atop-bound $CO_L$ in the 1950−2150 $cm^{-1}$ range as a function of potentials.



https://doi.org/10.1021/jacs.1c11253
J. Am. Chem. Soc. 2022, 144, 3039−3049

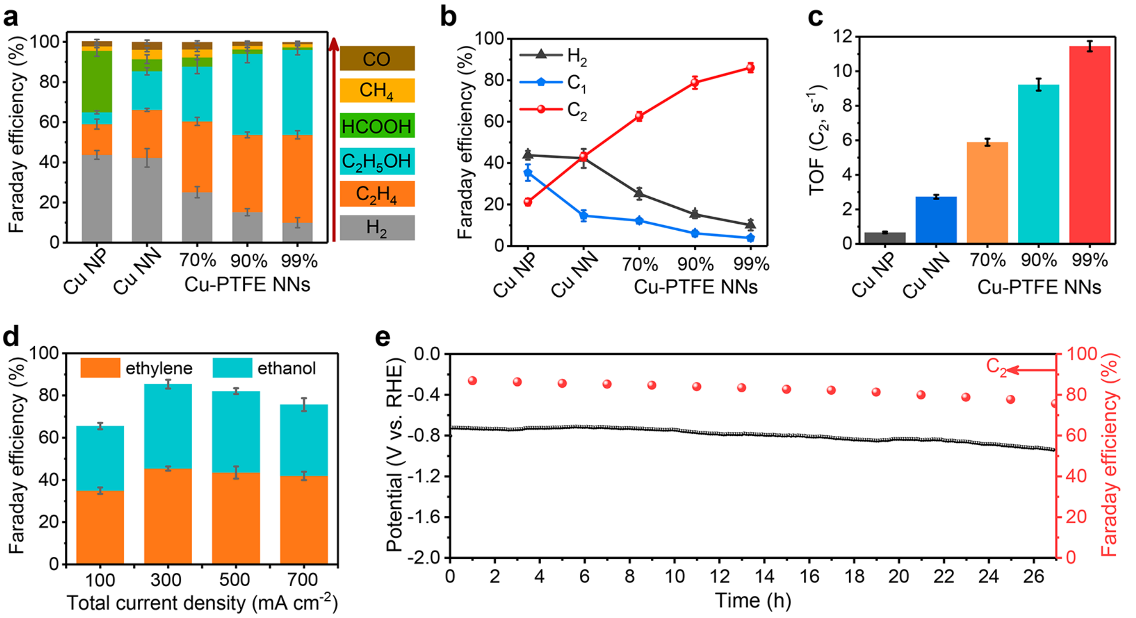


**Figure 4.** $CO_2$ electroreduction performance investigation. (a) Product distribution and corresponding FEs under the potential of −1.5 V vs RHE in a H-cell. (b) FEs of $C_2$, $C_1$, and $H_2$ products under the potential of −1.5 V vs RHE in a H-cell. (c) TOFs under the potential of −1.5 V vs RHE in a H-cell. (d) FEs of $C_2$ products on a Cu-PTFE-99 NN under different current densities in a flow cell. (e) Potential and FEs of $C_2$ products measured during 27 h of continuous operation at a current density of 300 mA $cm^{-2}$. Error bars correspond to the standard deviation of three independent electrode measurements.

$$\mathrm{TOF} = \frac{kT}{h} \times \exp\left(-\frac{\Delta E_a}{kT}\right)$$

where $k$ is the Boltzmann constant, $h$ is Planck's constant, $T$ is the temperature in Kelvin, and $\Delta E_a$ is the calculated activation energy of *CO dimerization. Similar to $\Delta G$, $\Delta E_a$ decreased with the increase of electric field, indicating that the electric field also favors $C_2$ generation kinetically (Figures S9 and S10 and Table S2). A TOF map of *CO dimerization at various electric fields and thermal fields shows that the TOF grows more than 2 orders of magnitude with the increase of the electric field and thermal field (Figure 1e). Obviously, the thermal field vastly improves the kinetics process of *CO dimerization (Figure S11). These findings predict that a locally enhanced electric−thermal field accelerates *CO dimerization both thermodynamically and kinetically (Figure 1f).

**Catalyst Synthesis and Characterization.** To probe our predictions experimentally, we prepared a suite of Cu NNs with PTFE coverage rates from 0 to 99% (Figure S12 and Table S3). Scanning electron microscopy (SEM) images reveal the obtained Cu samples have needle morphologies and visible PTFE layers on the needle bodies (Figure S13). Transmission electron microscopy (TEM), high-angle annular dark-field scanning TEM (HAADF-STEM), and energy-dispersive X-ray spectroscopy (EDX) elemental mapping analyses confirm the good PTFE coverage on the Cu NN bodies and only the top tip is exposed (Figure 2 and Figure S14).

To determine the morphological structure and chemical state of the tested catalysts, SEM and a series of spectroscopies were performed. Before the $CO_2$RR test, all catalysts were operated under a constant voltage of −1.4 V versus reversible hydrogen electrode (vs RHE) until the current was stable (Figure S15). SEM and EDX mapping images reveal that the catalysts retain the needle structure with good PTFE coverage after electroreduction (Figures S16 and S17). FTIR spectra of Cu-PTFE NNs before and after electroreduction show two visible characteristic peaks of PTFE located at 1100−1300 $cm^{-1}$ (Figure S18),[45] confirming the coverage of PTFE. X-ray diffraction (XRD) patterns and X-ray photoelectron spectroscopy (XPS) spectra (Figure S19) reveal that the Cu-PTFE NNs are metallic Cu after electroreduction,[46] which is further confirmed by the Cu K edge X-ray absorption near-edge spectra (XANES) and the extended X-ray absorption fine structure (XAFS) (Figure S20).[11,46]

**Effect of Tip-Induced Electric−Thermal Field.** To probe the enhanced electric field at the tips, we measured the concentration of adsorbed $K^+$ on the electrodes. The results show that Cu NN with a sharp tip structure has a higher $K^+$ concentration than that of the quasi-planar Cu NP, and the adsorbed $K^+$ concentration can be further enhanced when the Cu NN is covered with PTFE (Figures S21−S23 and Table S4). This finding indicates that the electric field of the Cu NN can be enhanced to about 7-fold by covering with PTFE (Figure 3a). We then probed the local thermal field by using an infrared thermal camera system. The temperature distribution on a single Cu needle electrode (Figure S24) shows a high temperature near the tip, indicating that the sharp tip can produce a local thermal field due to electron collision. Compared with a planar Cu NP, the pristine Cu NN shows about 4-fold higher temperature increment, and the temperature increment can be further enhanced to nearly 14-fold for a Cu-PTFE-99 NN (Figure 3b and Figures S25 and S26). These results (Figure 3a and b) indicate that the electric−thermal field at the tip can be improved by tuning the PTFE coverage, which is consistent with our theoretical simulations.

We then explored the capacity regarding adsorption and activation of $CO_2$ and CO molecules on Cu-PTFE NNs via gas electroresponse experiments (Figure S27). The results (Figure 3c and Figure S28) show that the $CO_2$ and CO adsorption responses become stronger with the increase of PTFE coverage, suggesting that the adsorption and activation of $CO_2$ and CO are


https://doi.org/10.1021/jacs.1c11253
J. Am. Chem. Soc. 2022, 144, 3039−3049

promoted by enhancing the tip-induced electric−thermal field.[9,47]

To further investigate how the tip-induced electric−thermal field modulates the adsorption and dimerization of *CO intermediates, *in situ* attenuated total reflection FTIR (ATR-FTIR, Figure S29) was conducted. The spectra show an obvious stretching band of linearly bonded CO ($CO_L$) in the range of 1950−2150 $cm^{-1}$ (Figure 3d and Figures S30−S32).[48−53] With the applied potentials stepping down from −0.2 to −0.9 V vs RHE, $CO_L$ stretching band areas increase gradually, indicating the *CO amount increased with the electric field (Figure 3e). Then, with the negative shift of the potential from −0.9 V to −1.5 V, $CO_L$ stretching band areas decreased with an accelerated rate as the PTFE coverage increased, indicating that the abundant *CO intermediates were consumed quickly to implement a fast *CO dimerization process under the enhanced thermal field (Figure S33, for details see the Supporting Information).[49,51] The time-resolved *in situ* ATR-FTIR spectra at the potential of −0.9 and −1.5 V vs RHE (Figures S34 and S35) confirmed that the *CO formation and dimerization processes were accelerated by increasing the electric field and thermal field, respectively. These findings demonstrate that the local electric−thermal field can enrich *CO intermediates on the active sites and accelerate *CO dimerization to produce $C_2$ products.

**Electrochemical $CO_2$ Reduction Performance.** To validate the enhancement of $CO_2$RR by tip-induced electric−thermal field, we evaluated the $CO_2$RR performance of these catalysts in a conventional H-cell with a $CO_2$-saturated 0.1 M $KHCO_3$ electrolyte (pH 6.8). We detected and analyzed the products under different potentials (Figure S36 and Table S5) through gas chromatography (GC) and NMR. The product distributions under a potential of −1.5 V vs RHE (Figure 4a) show that the main product for all Cu NN electrodes is $C_2$, whereas $C_1$ accounts for the majority of products on the Cu NP electrode. The FE of $C_2$ for a pristine Cu NN was 43.1 ± 1.9% at −1.5 V vs RHE, much higher than that of 21.2 ± 1.7% for a Cu NP. This value can be further enhanced with the increase of the PTFE coverage rate, and a $C_2$ FE of 86.1 ± 2.2% was obtained on the very top tip exposed Cu-PTFE-99 NN electrode (Figure 4b). This trend was retained even under a wide potential range (Figure S37 and Table S5), confirming that the tip-induced local electric−thermal field enhancement is favorable for $C_2$ generation versus $C_1$ and $H_2$ formation during $CO_2$RR.

To explore the intrinsic activity, we investigated the electrochemical surface areas (ECSAs) and current densities of all electrodes (Figures S38−S42 and Tables S6 and S7). ECSAs decreased with the increase of PTFE coverage rate as the active sites on the needle body were covered by PTFE. However, the partial current densities of $C_2$ increase with the PTFE coverage rate increasing and achieve a 4-fold enhancement for the very top tip exposed Cu-PTFE-99 NN compared with that of a pristine Cu NN.

To determine the activity per active site experimentally, we calculated the TOFs of $C_2$ production at the potential of −1.5 V vs RHE (Figures 4c, S43, S44 and Tables S8 and S9). Compared with a Cu NP, Cu-PTFE NNs exhibit higher TOFs, which increase with the PTFE coverage and reach a value of 11.5 ± 0.3 $s^{-1}$ Cu $site^{-1}$ at a Cu-PTFE-99 NN. This TOF value was about 5 times higher than that of a Cu NN (2.7 ± 0.1 $s^{-1}$ Cu $site^{-1}$) and outperformed the reported values, even ones for most single-atom catalysts (Table S10), proving the local electric−thermal field can greatly accelerate the $C_2$ formation during $CO_2$RR.

Then, we investigated the $CO_2$RR performance of Cu NN under different electrolyte temperatures. We found that enhancing the electrolyte temperature promotes the $CO_2$RR, but it is more favorable for $C_1$ and $H_2$ formation versus $C_2$ formation (Figure S45). Comparing the results of directly enhancing electrolyte temperature (heating the electrolyte to artificially enhance global temperature, denoted as electrolyte temperature) and locally enhancing the tip temperature (applying a potential to spontaneously enhance the local temperature at copper nanoneedle tips during $CO_2$RR, denoted as tip local temperature), we found that locally enhancing the tip temperature by tuning the PTFE coverage rate on the Cu NN body is more favorable for $C_2$ formation because it can directly act on $C_2$ active sites to accelerate *CO dimerization, rather than on $C_1$ or $H_2$ active sites to produce $C_1$ and $H_2$ (Figure S46).

To increase the gas reactant availability at the electrode surface, we also explored the $CO_2$RR performance in a flow cell (Figure S47). We deposited a Cu NP, a pristine Cu NN, and a Cu-PTFE-99 NN onto PTFE membrane gas-diffusion electrodes (GDEs) by spray coating and tested their $CO_2$RR activity in 1 M KOH. Among the samples, the Cu-PTFE-99 NN still exhibited the best activity and selectivity for $C_2$ production (Figures S48 and S49 and Table S11).

Next, we assessed the catalytic activity of the Cu-PTFE-99 NN in the current density range of 100−700 mA $cm^{-2}$ (Figures 4d, S50, and S51 and Tables S11 and S12). Under all tested current densities, the FEs for $C_2$ products were measured to be over 80%, indicating the promise for practical applications. Under the current density of 300 mA $cm^{-2}$, the best $C_2$ FE of 85.4 ± 1.5% was achieved with a partial current density of 256.2 ± 4.6 mA $cm^{-2}$ at a low overpotential of −0.77 V vs RHE. The calculated half-cell CEE of $C_2$ products was 49.3 ± 2.0% for the Cu-PTFE-99 NN (Figure S52 and Table S12), which approached the reported state-of-the-art catalysts (55% for Cu−Al alloys[10]). The Cu-PTFE-99 NN had a high stability in the flow cell with a total current density of 300 mA $cm^{-2}$ for over 25 h (Figure 4e). The very top tip exposed Cu-PTFE-99 NN catalyst approached or outperformed the reported state-of-the-art Cu-based catalysts (Table S13), benefiting from the synergistic promoting effect of the electric−thermal field.

## ■ CONCLUSION

In summary, we developed a strategy to accelerate the conversion of $CO_2$ to $C_2$ by a PTFE conformal coating on the Cu NN body to generate a locally enhanced electric−thermal field at the tip. Combining the theoretical studies and experimental investigations, we concluded that the electric−thermal field at the Cu NN tip can be controllably tuned by adjusting the coverage of PTFE on the body, and the locally enhanced electric−thermal field raised *CO intermediates and accelerated C−C coupling both thermodynamically and kinetically. Using this strategy, we achieved a $C_2$ FE of 85.4 ± 1.5% at a partial current density of more than 250 mA $cm^{-2}$ and a high TOF of 11.5 ± 0.3 $s^{-1}$ Cu $site^{-1}$ for $C_2$ generation. The findings suggest a new strategy for improving $CO_2$ conversion into value-added $C_2$ chemicals using renewable electricity with the aid of local electric−thermal field synergy. Considering the ease of fabrication and excellent scalability, we anticipate that this strategy—tuning the local electric−thermal field on the catalyst surface—may be generalized to promote other electrocatalytic reactions, by virtue of the unparalleled ability to enhance the electric field and temperature at the nanoscale.


https://doi.org/10.1021/jacs.1c11253
J. Am. Chem. Soc. 2022, 144, 3039−3049

## EXPERIMENTAL SECTION

**COMSOL Multiphysics Simulations.** In our work, the FEM model was constructed in COMSOL Multiphysics v 5.5 as a stationary, 2D axisymmetric model and consisted of a Cu needle, a PTFE layer, and an electrolyte diffusion layer. Conventional triangular meshes were used for all simulations, and the meshes were set to the densest grid around the electrode and PTFE surfaces. The MUMPS solver was used with a relative tolerance of 0.001.

The "Electric Currents" module was used to solve the electron density and electric field when the electrode is under a specific potential bias. The electric field, $E$, was computed as the negative gradient of the electric potential as follows:

$$E = -\nabla V$$

Additionally, Ohm's law was used to correlate the electric field to current density, $J$, as follows:

$$J = \sigma E$$

in which $\sigma$ is the electrical conductivity. The electrical conductivity of the copper electrode was set to be $5.998 \times 10^7$ S m$^{-1}$, while the PTFE layer conductivity and electrolyte conductivity were assumed to be $1 \times 10^{-15}$ and 10 S m$^{-1}$, respectively. The dielectric model was also used to relate the electric displacement, $D$, with the electric field as follows:

$$D = \varepsilon_0 \varepsilon_r E$$

where $\varepsilon_0$ represents the dielectric constant of the vacuum and $\varepsilon_r$ represents the dielectric constant of the materials (1 for Cu, 2.1 for PTFE, and 80 for the electrolyte). An electric potential (−1.3, −1.5, and −1.7 V) was applied to the bottom of the Cu needle, the ground was prescribed to the far side of the electrolyte, electric insulation was applied to the remaining electrolyte sides, and an initial value of 0 V was set everywhere.

The "Heat Transfer in Solids and Fluids" module was used to simulate the thermal field under different PTFE coverage rates. The heat transfer equation was used to estimate the thermal field in the system as a certain electric potential is applied.

$$\rho c_p u \cdot \nabla T + \nabla \cdot q = Q$$

Here, $\rho$ is density, $c_p$ is the specific heat capacity, $u$ is the velocity vector (estimated to be $1.667 \times 10^{-3}$ m s$^{-1}$), $T$ is temperature, $q$ is the heat flux, and $Q$ is a heat source term (equated with the heat generated due to the applied potential). The heat flux was calculated using the following equation:

$$q = -k\nabla T$$

in which $k$ is the thermal conductivity (401 W m$^{-1}$ K$^{-1}$ for Cu, 0.256 W m$^{-1}$ K$^{-1}$ for PTFE, and 0.599 W m$^{-1}$ K$^{-1}$ for the electrolyte). A reference and an initial temperature of 298 K were applied at the electrolyte and everywhere in the system, respectively.

**DFT Computational Details.** DFT calculations were performed with the PBE exchange−correlation functional and the projector augmented wave (PAW) method with the Vienna ab initio simulation package (VASP).[54−56] The energy cutoff of the plane wave was set to 400 eV, and 2 × 3 × 1 Monkhorst−Pack $k$ grids were used for the Brillouin-zone integrations. The electric field (from −0.8 to 0 V·Å$^{-1}$) along the $z$-axis was considered in our calculations. The convergence criteria for the iteration process were a maximal residual force less than 0.02 eV·Å$^{-1}$ and an energy change less than $10^{-5}$ eV. We employed the climbing image nudged elastic band method to find the transition states of CO coupling. The 5 × 3 supercell Cu(100) surface slab was built with three layers, including 45 Cu atoms. The bottom two layers were fixed and the top layer was relaxed. The vacuum layer was about 15 Å. Considering the effect of the solvent, six water molecules and one potassium atom were added near the surface.

**Materials.** Potassium hydroxide (KOH, ACS), potassium bicarbonate ($KHCO_3$, AR, 99.5%), polytetrafluoroethylene preparation (PTFE, 60 wt %), ammonium fluoride ($NH_4F$, AR, 98%), ammonium chloride ($NH_4Cl$, AR, 99.5%), sodium tetrachloroaurate(III) dihydrate ($NaAuCl_4 \cdot 2H_2O$), and sodium thiosulfate ($Na_2S_2O_3$, 99%) were purchased from Aladdin Industrial Corporation. Phosphoric acid ($H_3PO_4$, AR, 85%), copper sulfate ($CuSO_4 \cdot 5H_2O$, AR, 99%), citric acid ($H_3C_6H_5O_7$, AR, 99%), hydrochloric acid (HCl, GR, 38%), sulfuric acid ($H_2SO_4$, GR, 95−98%), hydrofluoric acid (HF, AR, ≥40%), hydrogen peroxide ($H_2O_2$, GR, ≥30%), sodium hydroxide (NaOH, AR, ≥96%), and sodium sulfite ($Na_2SO_3$, AR, ≥97%) were purchased from Sinopharm Chemical Reagent Co. Ltd. All reagents were used without further purification. Deionized water was used in the overall process of catalyst preparation and performance tests.

**Preparation of Cu NN and Cu-PTFE NN Electrodes.** First, $Cu(OH)_2$ NN electrodes were prepared by an anodized method.[57] Before anodizing, the bare Cu electrode was electropolished in a two-electrode system by using 85% $H_3PO_4$ solution as electrolyte, Cu foil as working electrode (0.5 × 0.35 cm$^{-2}$), and a platinum plate as counter electrode. A constant voltage of 4 V was applied to electropolish the Cu surface for 600 s. After polishing, the electrode was flushed with deionized water several times and dried with nitrogen gas flow. The obtained glossy Cu surface was then anodized in 3 M KOH electrolyte by using a polished Cu electrode as working electrode, a platinum plate as counter electrode, and Ag/AgCl (3.5 M KCl) as reference electrode. A constant current of 1 mA (∼5.7 mA cm$^{-2}$) was applied for 350 s to synthesize $Cu(OH)_2$ NNs.

Then, $Cu(OH)_2$ NNs with different PTFE coverage were prepared via a capillary percolation method. First, several scratches on the Cu substrate were constructed as channels to facilitate the transfer of PTFE solution. The PTFE solution (5 wt %, 2 μL) was dropwise added at the end of the scratches. The PTFE solution was permeated along with the scratches and then gradually diffused into $Cu(OH)_2$ NN arrays due to the capillary action. After complete diffusion, the excess PTFE solution was removed rapidly by dust-free paper and then dried naturally in air. The coverage rate of PTFE can be tuned by controlling the dosage of PTFE solution.

Finally, Cu NN and Cu-PTFE NN electrodes were obtained via an *in situ* electrochemical reduction process. Before the $CO_2$ electroreduction test, the as-prepared $Cu(OH)_2$ NN and $Cu(OH)_2$-PTFE NN electrodes were reduced under a constant potential of −1.4 V vs RHE for at least 180 s until the current become stable.

**Preparation of the Cu NP.** The Cu NP electrode was prepared through an electrodeposition approach. The Cu NPs were electrodeposited on Cu foil using a conventional two-electrode system, Cu foil substrate was used as the working electrode, and a graphite rod was used as a counter electrode. An aqueous solution of 0.1 M $CuSO_4 \cdot 5H_2O$ and 1 M citric acid was used as the electrolyte. The Cu NP was electrodeposited at a constant voltage of −1.5 V for 300 s. After the deposition, the samples were rinsed in distilled water and dried with nitrogen gas flow.

**Materials Characterization.** Phases of catalysts ware characterized by using XRD (Rigaku Miniflex 600, Cu Kα radiation with $\lambda$ = 1.514 84 Å) with a 2θ range from 5° to 80° and a scan rate of 8° min$^{-1}$. SEM images and EDX of the samples were obtained from a FEI Helios Nanolab 600 field emission electron microscope. TEM, HR-TEM, STEM, and corresponding EDX elemental mapping images were obtained from a FEI Tecnai G2 F20 field emission transmission electron microscope operated at 200 kV. XPS results were performed on a Thermo Fisher Scientific-Escalab 250Xi. All the binding energies were calibrated by the C 1s peak at 284.8 eV. FTIR and *in situ* electrochemical ATR-FTIR measurements were performed by using a Thermo iS50. The X-ray absorption spectroscopy measurements were conducted at Taiwan Beamlines BL01C1, BL07A1, and BL17C1 at the National Synchrotron Radiation Research Center (Hsinchu, Taiwan). The concentrations of adsorbed $K^+$ on electrodes were detected by using a Thermo Scientific ICS-600 ion chromatograph system. The temperatures on the electrode surface were measured through an infrared thermal camera (FLIR A615).

***In Situ* Electrochemical ATR-FTIR Measurements.** The *in situ* electrochemical ATR-FTIR measurements were performed using a thermoelectric IR spectrometer (Thermo Fisher IS50) equipped with a liquid $N_2$-cooled MCT-A detector.[58,59] A customized spectro-electrochemical cell was assembled on top of a Si prism to carry out the *in situ* testing process. A silicon prism crystal loaded with catalysts, a platinum


https://doi.org/10.1021/jacs.1c11253
J. Am. Chem. Soc. 2022, 144, 3039−3049

plate, and Ag/AgCl (saturated KCl solution filling) were used as the working electrode, counter electrode, and reference electrode, respectively. The $CO_2$-saturated 0.1 M $KHCO_3$ was used as electrolyte and purged with a constant flow (20 sccm) throughout the test to enable the balance of the test environment. In this work, the catalysts that were grown on Cu foil were scraped from substrate, then loaded on a Au film modified Si prism by using a drop-coating approach. Before catalyst loading, a Au film was deposited directly on the reflecting plane of the Si prism using a chemical deposition method.[58] First, the Si prism was polished with a slurry of 0.5 $\mu$m $Al_2O_3$ and sonicated in acetone and deionized water. After polishing, the Si prism was soaked in a piranha solution (3:1 volumetric ratio of 98% $H_2SO_4$ and $H_2O_2$) for 60 min in order to clean the prism of organic contaminants. Following cleaning, the reflecting plane of the Si prism was dried with a nitrogen gas flow and immersed in 40% $NH_4F$ solution for 150 s to create a hydrogen-terminated surface to improve adhesion of the Au film. Then the reflecting surface was immersed in a mixture of the Au plating solution (5.75 mM $NaAuCl_4 \cdot 2H_2O$ + 0.025 M $NH_4Cl$ + 0.075 M $Na_2SO_3$ + 0.025 M $Na_2S_2O_3$ + 0.026 M NaOH) and a 2 wt % HF solution (in a 4.4:1 ratio) at 55 °C for 10 min. After the deposition, the Au film was rinsed with deionized water and dried by nitrogen gas flow. The catalysts (200 mg) scraped from the Cu foil were dispersed in a hybrid solution including 750 $\mu$L of deionized water, 750 $\mu$L of alcohol, and 100 $\mu$L of Nafion (5 wt %). Then 100 $\mu$L of catalyst ink was cast onto the Au film modified Si prism reflecting surface. FTIR spectra were obtained from an average of 32 scans with a resolution of 8 $cm^{-1}$, and the range of wavenumbers of collected spectra was set from 1600 to 2400 $cm^{-1}$. The background spectrum was taken at the potential of +0.2 V vs RHE. The spectra depending on the potential were obtained by applying single potential steps and collected after running 90s. The time-resolved spectra were collected at a constant potential and collected every 15 s. Atop-bound CO ($CO_L$) bands are typically in the 1950−2100 $cm^{-1}$ region. Thus, the CO peak area calculations were performed by including the area under the curve between 1950 and 2100 $cm^{-1}$ to account for small shifts in the CO peak position because of changes in coverage, dipole coupling, or the impact of hydroxide adsorbed on adjacent sites.[52]

**Electrochemical Performance Measurements.** In this work, the $CO_2RR$ performance was investigated in a conventional H-cell and advanced flow cell. All the electrocatalytic measurements were carried out in a three-electrode system using an electrochemical station (AUT50783). All the potentials were measured against a Ag/AgCl (saturated KCl solution filling) reference electrode and converted to RHE as follows:

$$E_{RHE} = E_{Ag/AgCl} + 0.210 + 0.059 \times pH$$

In a H-cell, a Nafion-115 proton exchange membrane was used to separate the sealed cell. The as-prepared electrode, a Ag/AgCl (saturated KCl solution filling) electrode, and a platinum plate (2 × 2 $cm^2$) electrode were used as the working electrode, counter electrode, and reference electrode, respectively. The $CO_2$-saturated 0.1 M $KHCO_3$ solution was used as electrolyte (pH = 6.8). The cathodic compartment was continuously purged with a constant $CO_2$ (99.999%) flow rate (20 sccm) and vented directly into the gas-sampling loop of a GC. The electrolyte was collected and analyzed by NMR after the $CO_2RR$ test (electrolysis 45 min). The ECSAs of all electrodes were estimated by double-layer capacitance in $CO_2$-saturated 0.1 M $KHCO_3$. Non-Faradaic potential ranges were selected for all samples. The cyclic voltammograms (CVs) were measured at a potential window of 0.05−0.25 V vs RHE with different scan rates of 10, 20, 30, 40, 50, 60, 80, and 100 mV/s. The non-Faradaic current density was plotted against the scan rates, and the slope obtained was the double-layer capacitance ($C_{dl}$). The roughness factor of the catalysts was determined via $C_{dl}/C_s$, where $C_s$ represents the double-layer capacitance of a polycrystalline Cu electrode (Cu foil). For the lead UPD, a $N_2$-saturated 0.1 M $HClO_4$/10 mM $Pb(ClO_4)_2$ aqueous solution was used as the electrolyte. The potential was first set at −0.35 V vs Ag/AgCl for 150 s, and then cyclic voltammetry was recorded between −0.35 and 0 V vs Ag/AgCl at 10 mV $s^{-1}$.

In the flow cell, the PTFE membrane (pore size of 450 nm) electrode, nickel foam, and Ag/AgCl (saturated KCl solution filling) electrode were used as the cathode, anode, and reference electrode, respectively. To prepare the GDE (with a size of 2 × 2 $cm^2$), we first scraped the catalysts from the Cu foil, then deposited 10 mg of catalyst (mixed with 20 $\mu$L of 5 wt % Nafion in 1 mL of isopropanol) on the PTFE membrane with a loading mass about 2.5 mg $cm^{-2}$ by using an airbrush. All electrodes and the anion exchange membrane (Fumasep FAB-PK-130) were positioned and clamped together via PTFE gaskets. A 20 mL amount of electrolyte (1 M KOH, pH = 14) was circulated through both the anode and cathode chambers by two pumps with a flow rate of 10 mL $min^{-1}$. Meanwhile, $CO_2$ gas was continuously supplied to the gas chamber located at the back side of the cathode by using a mass flow controller with a flow rate of 20 mL $min^{-1}$. The performance of the cathodes was evaluated by performing constant-current electrolysis. The ohmic loss between the working and reference electrodes was measured using the electrochemical impedance spectroscopy technique (with a potentiostatic mode in the frequency range of $10^5$ to 0.1 Hz) at the ending of the electrolysis, and 80% *iR* compensation (*i*, current; *R*, uncompensated resistance) was applied to correct the potentials manually.

**$CO_2$ Reduction Products Analysis.** Gas products were analyzed by GC and quantification via an external standard method. Each peak in GC corresponds to a product, and concentration ($V$) is proportional to peak area. The FEs of gas products were calculated using the equation

$$FE = \frac{V \times Q \times P \times nF}{R \times T \times i_{total}} \times 100$$

where $V$ is the volume concentration from GC, $i$ is the current recorded by the workstation, $P$ is pressure, $F$ is the Faradaic constant, 96 485 C $mol^{-1}$, $R$ is the ideal gas constant, 8.314 $m^3 \cdot Pa\ (K \cdot mol)^{-1}$, $Q$ is flow rate, 20 mL $min^{-1}$, and $T$ is temperature.

Liquid products were analyzed by NMR. Concentration ($C_{liquid}$) was obtained from NMR, $V$ is electrolyte volume, $F$ is the Faradaic constant, $Q_{total}$ is the electricity record by the workstation. The FEs of liquid products were calculated using the equation

$$FE = \frac{C_{liquid} \times V \times nF}{Q_{total}} \times 100$$

In the flow cell, the half-cell CEE for ethylene and ethanol can be calculated as follows:[13,15]

$$CEE = \frac{(1.23 + (-E_{ethylene})) \times FE_{ethylene}}{(1.23 + (-E_{applied}))} + \frac{(1.23 + (-E_{ethanol})) \times FE_{ethanol}}{(1.23 + (-E_{applied}))}$$

Here, the overpotential of oxygen evolution in the anode is assumed to be zero. $E_{applied}$ is the measured potential values in the experiment, $FE_{ethylene}$ and $FE_{ethanol}$ are the measured Faradaic efficiency of ethylene and ethanol in percentage, $E_{ethylene}$ = 0.08 V vs RHE, and $E_{ethanol}$ = 0.09 V vs RHE for the $CO_2RR$.

**Adsorbed $K^+$ Measurement.** The concentrations of adsorbed $K^+$ on electrodes were performed in 0.1 M $KHCO_3$ solution by using a three-electrode system and an ion chromatograph (IC, Thermo Scientific ICS-600). All the electrodes were run in 0.1 M $KHCO_3$ solution with an applied voltage at −1.5 V vs RHE. Once the running time reached 120 s, the electrode was directly raised above the electrolyte. Next, the electrodes were transferred with voltage and immersed in 10 mL of pure water, then the applied potential was removed and shaking was performed for 1 min in pure water, to enable the adsorbed $K^+$ on the surface of catalysts to be completely released into the pure water. After repeating the above process 10 times, the concentration of $K^+$ in the water was checked using an IC. The XPS of bare Cu NN and Cu-PTFE-99 NN under the conditions of before and after releasing $K^+$ was measured.

**Electrode Surface Temperature Measurement.** The temperature on the electrode surface was measured by an infrared thermal


https://doi.org/10.1021/jacs.1c11253
J. Am. Chem. Soc. 2022, 144, 3039−3049

camera (FLIR A615). The electrodes with an exposed area of 1 × 1 $cm^{-2}$ were prepared using the same procedure as we described in previous methods. The as-prepared electrode was connected with DC power (Luyang, YB1731B). The temperature distribution on the electrode's surface was collected under an applied constant current. We also measured the temperature on macroscopic Cu needle electrodes using the same procedure.

**$CO_2$ and CO Adsorption Test.** The $CO_2$ (or CO) adsorption on the catalyst's surface was characterized by a self-designed gas adsorption electroresponse device.[47] The electrodes with an exposed area of 1 × 1 $cm^{-2}$ were prepared using the same procedure as we described in previous methods. The as-prepared electrode was connected with the electrochemical workstation (CHI 660E) and put into a sealed container. This sealed container was connected with a vacuum pump and $CO_2$ (or CO) alimentative system. Before the $CO_2$ (or CO) adsorption electroresponse test, the sealed container kept the vacuum state by the working of a vacuum pump. The curve of current as a function of time was monitored through multipotential steps (0 V, −0.05 V, −0.10 V) in the vacuum state, and each potential was run for 10 s. Then $CO_2$ (or CO) gas was injected into the sealed container. The curve of the current as a function of time was monitored again under the same potentials and running time. Due to the adsorption of $CO_2$ (or CO) on the catalyst's surface, the current response was changed. From the difference of current density ($\Delta j = j_{gas} - j_{Vacuum}$) under the vacuum state ($j_{Vacuum}$) and $CO_2$ (or CO) atmosphere ($j_{gas}$), we can quantify the adsorbed capacity of $CO_2$ (or CO) on the catalyst's surface.

**Turnover Frequency Calculations.** The experimental TOFs of $C_2$ production on a single Cu active site were calculated by using the following equation:

$$\mathrm{TOF} = \frac{j_{Geo} \times S}{1000 \times 12 \times n_{Cu} \times F}$$

where $j_{Geo}$ is the geometric current density (mA $cm^{-2}$) of ethylene and ethanol, $S$ is the electrode geometric area (0.175 $cm^2$), 12 is the number of consumed electrons for producing an ethylene (or ethanol) molecule, $n_{Cu}$ is the mole number of surface Cu atoms (mol), and $F$ is the Faraday constant (96485.3 C $mol^{-1}$). To estimate the number of active Cu atoms on the catalyst surface, we proposed an approximate catalyst structure model based on SEM results.

For the single Cu NP model, the surface area was calculated from

$$S_{CuNP} = \frac{3}{4} \times 4\pi R^2 = 3.39 \times 10^{-12}\ \mathrm{m}^2$$

For the single Cu NN model, the surface area was calculated from

$$S_{CuNN} = \pi r l = 9.42 \times 10^{-12}\ \mathrm{m}^2$$

Based on the surface the atomic density of Cu being $C_{Cu} = 1.47 \times 10^{19}$ $m^{-2}$, the number of surface Cu atom on each Cu NP and Cu NN can be calculated as follows:

$$N_{CuNP} = S_{CuNP} \times C_{Cu} = 1.38 \times 10^8$$

$$N_{CuNN} = S_{CuNN} \times 4\pi R^2 = 4.98 \times 10^7$$

To obtain the density of nanoneedles ($D_{Cu\ NN}$) and nanoparticles ($D_{Cu\ NP}$) on the electrodes, the representative SEM results were statistically analyzed, and we calculated $D_{Cu\ NN}$ = 0.4772 $\mu m^{-2}$ and $D_{Cu\ NP}$ = 1.0352 $\mu m^{-2}$. On the basis of these parameters, we can calculate the mole number of active Cu atoms on surface ($n_{Cu}$) using the following equation:

$$n_{Cu} = \frac{\mathrm{D} \times S \times 10^8 \times N}{N_A} \times k$$

where $D$ is the density of nanoneedles ($D_{Cu\ NN}$) and nanoparticles ($D_{Cu\ NP}$) on the electrodes, $S$ is the electrode geometric area (0.175 $cm^2$), $N$ is the number of surface Cu atoms on each Cu NN ($N_{Cu\ NN}$) and Cu NP ($N_{Cu\ NP}$), $k$ is the correction factor of the active area (obtained from ECSA), and $N_A$ is the Avogadro constant ($6.02 \times 10^{23}$). For all Cu nanoneedle electrodes, $D_{Cu\ NN}$ and $N_{Cu\ NN}$ are identical. For Cu NN and Cu NP electrodes, $k$ = 1; for a Cu-PTFE-1 NN electrode, $k$ = 0.62; for a Cu-PTFE-3 NN electrode, $k$ = 0.46; for a Cu-PTFE-5 NN electrode, $k$ = 0.37.

## ■ ASSOCIATED CONTENT

### Supporting Information

The Supporting Information is available free of charge at https://pubs.acs.org/doi/10.1021/jacs.1c11253.

Additional theoretical calculations, characterizations, and catalytic performance results (PDF)

## ■ AUTHOR INFORMATION


### Corresponding Authors

**Stefan A. Maier** − *Chair in Hybrid Nanosystems, Nanoinstitute Munich, Faculty of Physics, Ludwig-Maximilians-Universität München, D-80539 München, Germany; Department of Physics, Imperial College London, London SW7 2AZ, U.K.;* orcid.org/0000-0001-9704-7902; Email: Stefan.Maier@physik.uni-muenchen.de

**Min Liu** − *Hunan Joint International Research Center for Carbon Dioxide Resource Utilization, State Key Laboratory of Powder Metallurgy, School of Physical and Electronics, Central South University, Changsha 410083, China;* orcid.org/0000-0002-9007-4817; Email: minliu@csu.edu.cn

### Authors

**Baopeng Yang** − *Hunan Joint International Research Center for Carbon Dioxide Resource Utilization, State Key Laboratory of Powder Metallurgy, School of Physical and Electronics, Central South University, Changsha 410083, China*

**Kang Liu** − *Hunan Joint International Research Center for Carbon Dioxide Resource Utilization, State Key Laboratory of Powder Metallurgy, School of Physical and Electronics, Central South University, Changsha 410083, China;* orcid.org/0000-0002-8781-7747

**HuangJingWei Li** − *Hunan Joint International Research Center for Carbon Dioxide Resource Utilization, State Key Laboratory of Powder Metallurgy, School of Physical and Electronics, Central South University, Changsha 410083, China*

**Changxu Liu** − *Chair in Hybrid Nanosystems, Nanoinstitute Munich, Faculty of Physics, Ludwig-Maximilians-Universität München, D-80539 München, Germany*

**Junwei Fu** − *Hunan Joint International Research Center for Carbon Dioxide Resource Utilization, State Key Laboratory of Powder Metallurgy, School of Physical and Electronics, Central South University, Changsha 410083, China;* orcid.org/0000-0003-0190-1663

**Hongmei Li** − *Hunan Joint International Research Center for Carbon Dioxide Resource Utilization, State Key Laboratory of Powder Metallurgy, School of Physical and Electronics, Central South University, Changsha 410083, China*

**Jianan Erick Huang** − *Department of Electrical and Computer Engineering, University of Toronto, Toronto, Ontario M5S 1A4, Canada*

**Pengfei Ou** − *Department of Electrical and Computer Engineering, University of Toronto, Toronto, Ontario M5S 1A4, Canada;* orcid.org/0000-0002-3630-0385

**Tartela Alkayyali** − *Department of Mechanical and Industrial Engineering, University of Toronto, Toronto, Ontario M5S 3G8, Canada;* orcid.org/0000-0003-3895-8700

**Chao Cai** − *Hunan Joint International Research Center for Carbon Dioxide Resource Utilization, State Key Laboratory of*

Powder Metallurgy, School of Physical and Electronics, Central South University, Changsha 410083, China; orcid.org/0000-0002-3695-3247

**Yuxia Duan** – *Hunan Joint International Research Center for Carbon Dioxide Resource Utilization, State Key Laboratory of Powder Metallurgy, School of Physical and Electronics, Central South University, Changsha 410083, China*

**Hui Liu** – *School of Metallurgy and Environment, Central South University, Changsha 410083, China;* orcid.org/0000-0003-2693-2546

**Pengda An** – *School of Materials Science and Engineering, Central South University, Changsha 410083, China*

**Ning Zhang** – *School of Materials Science and Engineering, Central South University, Changsha 410083, China;* orcid.org/0000-0002-3033-0276

**Wenzhang Li** – *School of Chemistry and Chemical Engineering, Central South University, Changsha 410083, China;* orcid.org/0000-0002-6801-4105

**Xiaoqing Qiu** – *School of Chemistry and Chemical Engineering, Central South University, Changsha 410083, China;* orcid.org/0000-0003-4655-4730

**Chuankun Jia** – *College of Materials Science and Engineering, Changsha University of Science & Technology, Changsha 410114, China*

**Junhua Hu** – *School of Materials Science and Engineering, Zhengzhou University, Zhengzhou 450002, China;* orcid.org/0000-0003-0191-1503

**Liyuan Chai** – *School of Metallurgy and Environment, Central South University, Changsha 410083, China*

**Zhang Lin** – *School of Metallurgy and Environment, Central South University, Changsha 410083, China;* orcid.org/0000-0002-6600-2055

**Yongli Gao** – *Department of Physics and Astronomy, University of Rochester, Rochester, New York 14627, United States;* orcid.org/0000-0001-9765-5246

**Masahiro Miyauchi** – *Department of Materials Science and Engineering, School of Materials and Chemical Technology, Tokyo Institute of Technology, Tokyo 152-8552, Japan;* orcid.org/0000-0001-8889-2645

**Emiliano Cortés** – *Chair in Hybrid Nanosystems, Nanoinstitute Munich, Faculty of Physics, Ludwig-Maximilians-Universität München, D-80539 München, Germany;* orcid.org/0000-0001-8248-4165

Complete contact information is available at: https://pubs.acs.org/10.1021/jacs.1c11253

### Author Contributions

[#]B.Y., K.Li., H.-J.W.L., and C.L. contributed equally.

### Notes

The authors declare no competing financial interest.

## ACKNOWLEDGMENTS

This work was supported by the Natural Science Foundation of China (Grant Nos. 21872174, 22002189, 22011530423, and U1932148), Technology Cooperation Program (Grant Nos. 2017YFE0127800 and 2018YFE0203400), Hunan Provincial Key Research and Development Program (2020WK2002), Hunan Provincial Natural Science Foundation of China (2020JJ2041 and 2020JJ5691), Hunan Provincial Science and Technology Program (2017XK2026), Shenzhen Science and Technology Innovation Project (Grant No. JCYJ20180307151313532), National Postdoctoral Program for Innovative Talents of China, Postdoctoral Science Foundation of China (Grant No. 2018M640759), Thousand Youth Talents Plan of China and Hundred Youth Talents Program of Hunan, the Hunan Provincial Science and Technology Plan Project (Grant No. 2017TP1001), the Outstanding Youth Exchange Program of China Association for Science and Technology (Grant No. 2018CASTQNJL56), and Fundamental Research Funds for the Central Universities of Central South University (2021zzts0060). We thank Prof. Edward Sargent and Dr. Joshua Wicks for helpful discussions. We acknowledge financial support from the Deutsche Forschungsgemeinschaft (DFG, German Research Foundation) under grant numbers EXC 2089/1 – 390776260 (Germany´s Excellence Strategy), the Bavarian State Ministry of Science, Research, and Arts through the program "Solar Technologies Go Hybrid (SolTech)" and the European Commission through the ERC Starting Grant CATALIGHT (802989). S.M. additionally acknowledges the Lee-Lucas Chair in Physics as well as the Engineering and Physical Sciences Research Council (EPSRC UK).

## REFERENCES

(1) De Luna, P.; Hahn, C.; Higgins, D.; Jaffer, S. A.; Jaramillo, T. F.; Sargent, E. H. What Would It Take for Renewably Powered Electrosynthesis to Displace Petrochemical Processes? *Science* **2019**, *364* (6438), eaav3506.

(2) Bushuyev, O. S.; De Luna, P.; Dinh, C. T.; Tao, L.; Saur, G.; van de Lagemaat, J.; Kelley, S. O.; Sargent, E. H. What Should We Make with $CO_2$ and How Can We Make It? *Joule* **2018**, *2* (5), 825–832.

(3) Gür, T. M. Review of Electrical Energy Storage Technologies, Materials and Systems: Challenges and Prospects for Large-Scale Grid Storage. *Energy Environ. Sci.* **2018**, *11* (10), 2696–2767.

(4) Gao, D.; Arán-Ais, R. M.; Jeon, H. S.; Roldan Cuenya, B. Rational Catalyst and Electrolyte Design for $CO_2$ Electroreduction towards Multicarbon Products. *Nat. Catal.* **2019**, *2* (3), 198–210.

(5) Birdja, Y. Y.; Pérez-Gallent, E.; Figueiredo, M. C.; Göttle, A. J.; Calle-Vallejo, F.; Koper, M. T. M. Advances and Challenges in Understanding the Electrocatalytic Conversion of Carbon Dioxide to Fuels. *Nat. Energy* **2019**, *4* (9), 732–745.

(6) Nitopi, S.; Bertheussen, E.; Scott, S. B.; Liu, X.; Engstfeld, A. K.; Horch, S.; Seger, B.; Stephens, I. E. L.; Chan, K.; Hahn, C.; Nørskov, J. K.; Jaramillo, T. F.; Chorkendorff, I. Progress and Perspectives of Electrochemical $CO_2$ Reduction on Copper in Aqueous Electrolyte. *Chem. Rev.* **2019**, *119* (12), 7610–7672.

(7) Wang, G.; Chen, J.; Ding, Y.; Cai, P.; Yi, L.; Li, Y.; Tu, C.; Hou, Y.; Wen, Z.; Dai, L. Electrocatalysis for $CO_2$ Conversion: From Fundamentals to Value-Added Products. *Chem. Soc. Rev.* **2021**, *50* (8), 4993–5061.

(8) Ross, M. B.; De Luna, P.; Li, Y.; Dinh, C. T.; Kim, D.; Yang, P.; Sargent, E. H. Designing Materials for Electrochemical Carbon Dioxide Recycling. *Nat. Catal.* **2019**, *2* (8), 648–658.

(9) Zhou, Y.; Che, F.; Liu, M.; Zou, C.; Liang, Z.; De Luna, P.; Yuan, H.; Li, J.; Wang, Z.; Xie, H.; Li, H.; Chen, P.; Bladt, E.; Quintero-Bermudez, R.; Sham, T. K.; Bals, S.; Hofkens, J.; Sinton, D.; Chen, G.; Sargent, E. H. Dopant-Induced Electron Localization Drives $CO_2$ Reduction to $C_2$ Hydrocarbons. *Nat. Chem.* **2018**, *10* (9), 974–980.

(10) Zhong, M.; Tran, K.; Min, Y.; Wang, C.; Wang, Z.; Dinh, C. T.; De Luna, P.; Yu, Z.; Rasouli, A. S.; Brodersen, P.; Sun, S.; Voznyy, O.; Tan, C. S.; Askerka, M.; Che, F.; Liu, M.; Seifitokaldani, A.; Pang, Y.; Lo, S. C.; Ip, A.; Ulissi, Z.; Sargent, E. H. Accelerated Discovery of $CO_2$ Electrocatalysts Using Active Machine Learning. *Nature* **2020**, *581* (7807), 178–183.

(11) De Luna, P.; Quintero-Bermudez, R.; DInh, C. T.; Ross, M. B.; Bushuyev, O. S.; Todorović, P.; Regier, T.; Kelley, S. O.; Yang, P.; Sargent, E. H. Catalyst Electro-Redeposition Controls Morphology and Oxidation State for Selective Carbon Dioxide Reduction. *Nat. Catal.* **2018**, *1* (2), 103–110.



https://doi.org/10.1021/jacs.1c11253
J. Am. Chem. Soc. 2022, 144, 3039–3049

(12) De Gregorio, G. L.; Burdyny, T.; Loiudice, A.; Iyengar, P.; Smith, W. A.; Buonsanti, R. Facet-Dependent Selectivity of Cu Catalysts in Electrochemical $CO_2$ Reduction at Commercially Viable Current Densities. *ACS Catal.* **2020**, *10* (9), 4854−4862.

(13) Wang, Y.; Wang, Z.; Dinh, C. T.; Li, J.; Ozden, A.; Golam Kibria, M.; Seifitokaldani, A.; Tan, C. S.; Gabardo, C. M.; Luo, M.; Zhou, H.; Li, F.; Lum, Y.; McCallum, C.; Xu, Y.; Liu, M.; Proppe, A.; Johnston, A.; Todorovic, P.; Zhuang, T. T.; Sinton, D.; Kelley, S. O.; Sargent, E. H. Catalyst Synthesis under $CO_2$ Electroreduction Favours Faceting and Promotes Renewable Fuels Electrosynthesis. *Nat. Catal.* **2020**, *3* (2), 98−106.

(14) Li, F.; Thevenon, A.; Rosas-Hernández, A.; Wang, Z.; Li, Y.; Gabardo, C. M.; Ozden, A.; Dinh, C. T.; Li, J.; Wang, Y.; Edwards, J. P.; Xu, Y.; McCallum, C.; Tao, L.; Liang, Z. Q.; Luo, M.; Wang, X.; Li, H.; O'Brien, C. P.; Tan, C. S.; Nam, D. H.; Quintero-Bermudez, R.; Zhuang, T. T.; Li, Y. C.; Han, Z.; Britt, R. D.; Sinton, D.; Agapie, T.; Peters, J. C.; Sargent, E. H. Molecular Tuning of $CO_2$-to-Ethylene Conversion. *Nature* **2020**, *577* (7791), 509−513.

(15) Wang, X.; Wang, Z.; García de Arquer, F. P.; Dinh, C. T.; Ozden, A.; Li, Y. C.; Nam, D. H.; Li, J.; Liu, Y. S.; Wicks, J.; Chen, Z.; Chi, M.; Chen, B.; Wang, Y.; Tam, J.; Howe, J. Y.; Proppe, A.; Todorović, P.; Li, F.; Zhuang, T. T.; Gabardo, C. M.; Kirmani, A. R.; McCallum, C.; Hung, S. F.; Lum, Y.; Luo, M.; Min, Y.; Xu, A.; O'Brien, C. P.; Stephen, B.; Sun, B.; Ip, A. H.; Richter, L. J.; Kelley, S. O.; Sinton, D.; Sargent, E. H. Efficient Electrically Powered $CO_2$-to-Ethanol via Suppression of Deoxygenation. *Nat. Energy* **2020**, *5* (6), 478−486.

(16) Wang, H.; Tzeng, Y. K.; Ji, Y.; Li, Y.; Li, J.; Zheng, X.; Yang, A.; Liu, Y.; Gong, Y.; Cai, L.; Li, Y.; Zhang, X.; Chen, W.; Liu, B.; Lu, H.; Melosh, N. A.; Shen, Z. X.; Chan, K.; Tan, T.; Chu, S.; Cui, Y. Synergistic Enhancement of Electrocatalytic $CO_2$ Reduction to $C_2$ Oxygenates at Nitrogen-Doped Nanodiamonds/Cu Interface. *Nat. Nanotechnol.* **2020**, *15* (2), 131−137.

(17) Pang, Y.; Li, J.; Wang, Z.; Tan, C. S.; Hsieh, P. L.; Zhuang, T. T.; Liang, Z. Q.; Zou, C.; Wang, X.; De Luna, P.; Edwards, J. P.; Xu, Y.; Li, F.; Dinh, C. T.; Zhong, M.; Lou, Y.; Wu, D.; Chen, L. J.; Sargent, E. H.; Sinton, D. Efficient Electrocatalytic Conversion of Carbon Monoxide to Propanol Using Fragmented Copper. *Nat. Catal.* **2019**, *2* (3), 251−258.

(18) Liu, M.; Liu, M.; Wang, X.; Kozlov, S. M.; Cao, Z.; De Luna, P.; Li, H.; Qiu, X.; Liu, K.; Hu, J.; Jia, C.; Wang, P.; Zhou, H.; He, J.; Zhong, M.; Lan, X.; Zhou, Y.; Wang, Z.; Li, J.; Seifitokaldani, A.; Dinh, C. T.; Liang, H.; Zou, C.; Zhang, D.; Yang, Y.; Chan, T. S.; Han, Y.; Cavallo, L.; Sham, T. K.; Hwang, B. J.; Sargent, E. H. Quantum-Dot-Derived Catalysts for $CO_2$ Reduction Reaction. *Joule* **2019**, *3* (7), 1703−1718.

(19) Zhuang, T. T.; Liang, Z. Q.; Seifitokaldani, A.; Li, Y.; De Luna, P.; Burdyny, T.; Che, F.; Meng, F.; Min, Y.; Quintero-Bermudez, R.; Dinh, C. T.; Pang, Y.; Zhong, M.; Zhang, B.; Li, J.; Chen, P. N.; Zheng, X. L.; Liang, H.; Ge, W. N.; Ye, B. J.; Sinton, D.; Yu, S. H.; Sargent, E. H. Steering Post-C-C Coupling Selectivity Enables High Efficiency Electroreduction of Carbon Dioxide to Multi-Carbon Alcohols. *Nat. Catal.* **2018**, *1* (6), 421−428.

(20) Liu, M.; Pang, Y.; Zhang, B.; De Luna, P.; Voznyy, O.; Xu, J.; Zheng, X.; Dinh, C. T.; Fan, F.; Cao, C.; de Arquer, F. P. G.; Safaei, T. S.; Mepham, A.; Klinkova, A.; Kumacheva, E.; Filleter, T.; Sinton, D.; Kelley, S. O.; Sargent, E. H. Enhanced Electrocatalytic $CO_2$ Reduction via Field-Induced Reagent Concentration. *Nature* **2016**, *537* (7620), 382−386.

(21) Chen, L. D.; Urushihara, M.; Chan, K.; Nørskov, J. K. Electric Field Effects in Electrochemical $CO_2$ Reduction. *ACS Catal.* **2016**, *6* (10), 7133−7139.

(22) Che, F.; Gray, J. T.; Ha, S.; Kruse, N.; Scott, S. L.; McEwen, J.-S. Elucidating the Roles of Electric Fields in Catalysis: A Perspective. *ACS Catal.* **2018**, *8* (6), 5153−5174.

(23) Liu, P.; Chen, B.; Liang, C.; Yao, W.; Cui, Y.; Hu, S.; Zou, P.; Zhang, H.; Fan, H. J.; Yang, C. Tip-Enhanced Electric Field: A New Mechanism Promoting Mass Transfer in Oxygen Evolution Reactions. *Adv. Mater.* **2021**, *33* (9), 1−9.

(24) Gao, F.; Hu, S.; Zhang, X.; Zheng, Y.; Wang, H.; Niu, Z.; Yang, P.; Bao, R.; Ma, T.; Dang, Z.; Guan, Y.; Zheng, X.; Zheng, X.; Zhu, J.; Gao, M.; Yu, S. High-Curvature Transition-Metal Chalcogenide Nanostructures with a Pronounced Proximity Effect Enable Fast and Selective $CO_2$ Electroreduction. *Angew. Chem., Int. Ed.* **2020**, *132* (22), 8784−8790.

(25) Nairan, A.; Liang, C.; Chiang, S.-W.; Wu, Y.; Zou, P.; Khan, U.; Liu, W.; Kang, F.; Guo, S.; Wu, J.; Yang, C. Proton Selective Adsorption on Pt−Ni Nano-Thorn Array Electrodes for Superior Hydrogen Evolution Activity. *Energy Environ. Sci.* **2021**, *14* (3), 1594−1601.

(26) Jiang, H.; Hou, Z.; Luo, Y. Unraveling the Mechanism for the Sharp-Tip Enhanced Electrocatalytic Carbon Dioxide Reduction: The Kinetics Decide. *Angew. Chem., Int. Ed.* **2017**, *56* (49), 15617−15621.

(27) Shetty, M.; Ardagh, M. A.; Pang, Y.; Abdelrahman, O. A.; Dauenhauer, P. J. Electric-Field-Assisted Modulation of Surface Thermochemistry. *ACS Catal.* **2020**, *10* (21), 12867−12880.

(28) Robatjazi, H.; Zhao, H.; Swearer, D. F.; Hogan, N. J.; Zhou, L.; Alabastri, A.; McClain, M. J.; Nordlander, P.; Halas, N. J. Plasmon-Induced Selective Carbon Dioxide Conversion on Earth-Abundant Aluminum-Cuprous Oxide Antenna-Reactor Nanoparticles. *Nat. Commun.* **2017**, *8* (1), 27.

(29) Zhang, X.; Li, X.; Zhang, D.; Su, N. Q.; Yang, W.; Everitt, H. O.; Liu, J. Product Selectivity in Plasmonic Photocatalysis for Carbon Dioxide Hydrogenation. *Nat. Commun.* **2017**, *8* (1), 14542.

(30) Chen, Y.; DeGlee, B.; Tang, Y.; Wang, Z.; Zhao, B.; Wei, Y.; Zhang, L.; Yoo, S.; Pei, K.; Kim, J. H.; Ding, Y.; Hu, P.; Tao, F. F.; Liu, M. A Robust Fuel Cell Operated on Nearly Dry Methane at 500°C Enabled by Synergistic Thermal Catalysis and Electrocatalysis. *Nat. Energy* **2018**, *3* (12), 1042−1050.

(31) Niether, C.; Faure, S.; Bordet, A.; Deseure, J.; Chatenet, M.; Carrey, J.; Chaudret, B.; Rouet, A. Improved Water Electrolysis Using Magnetic Heating of FeC−Ni Core−Shell Nanoparticles. *Nat. Energy* **2018**, *3* (6), 476−483.

(32) Zhou, S.; Yang, X.; Xu, X.; Dou, S. X.; Du, Y.; Zhao, J. Boron Nitride Nanotubes for Ammonia Synthesis: Activation by Filling Transition Metals. *J. Am. Chem. Soc.* **2020**, *142* (1), 308−317.

(33) Clark, E. L.; Ringe, S.; Tang, M.; Walton, A.; Hahn, C.; Jaramillo, T. F.; Chan, K.; Bell, A. T. Influence of Atomic Surface Structure on the Activity of Ag for the Electrochemical Reduction of $CO_2$ to CO. *ACS Catal.* **2019**, *9* (5), 4006−4014.

(34) Hartschuh, A. Tip-Enhanced near-Field Optical Microscopy. *Angew. Chem., Int. Ed.* **2008**, *47* (43), 8178−8191.

(35) D'Agosta, R.; Sai, N.; Di Ventra, M. Local Electron Heating in Nanoscale Conductors. *Nano Lett.* **2006**, *6* (12), 2935−2938.

(36) Downes, A.; Salter, D.; Elfick, A. Heating Effects in Tip-Enhanced Optical Microscopy. *Opt. Express* **2006**, *14* (12), 5216.

(37) Jin, C. Y.; Li, Z.; Williams, R. S.; Lee, K. C.; Park, I. Localized Temperature and Chemical Reaction Control in Nanoscale Space by Nanowire Array. *Nano Lett.* **2011**, *11* (11), 4818−4825.

(38) Kortlever, R.; Shen, J.; Schouten, K. J. P.; Calle-Vallejo, F.; Koper, M. T. M. Catalysts and Reaction Pathways for the Electrochemical Reduction of Carbon Dioxide. *J. Phys. Chem. Lett.* **2015**, *6* (20), 4073−4082.

(39) Todorova, T. K.; Schreiber, M. W.; Fontecave, M. Mechanistic Understanding of $CO_2$ Reduction Reaction ($CO_2$RR) Toward Multicarbon Products by Heterogeneous Copper-Based Catalysts. *ACS Catal.* **2020**, *10* (3), 1754−1768.

(40) Bagger, A.; Ju, W.; Varela, A. S.; Strasser, P.; Rossmeisl, J. Electrochemical $CO_2$ Reduction: Classifying Cu Facets. *ACS Catal.* **2019**, *9* (9), 7894−7899.

(41) Iyengar, P.; Kolb, M. J.; Pankhurst, J. R.; Calle-Vallejo, F.; Buonsanti, R. Elucidating the Facet-Dependent Selectivity for $CO_2$ Electroreduction to Ethanol of Cu-Ag Tandem Catalysts. *ACS Catal.* **2021**, *11* (8), 4456−4463.

(42) Charnay, B. P.; Cui, Z.; Marx, M. A.; Palazzo, J.; Co, A. C. Insights into the $CO_2$ Reduction Pathway through the Electrolysis of Aldehydes on Copper. *ACS Catal.* **2021**, *11* (7), 3867−3876.

(43) Montoya, J. H.; Shi, C.; Chan, K.; Nørskov, J. K. Theoretical Insights into a CO Dimerization Mechanism in $CO_2$ Electroreduction. *J. Phys. Chem. Lett.* **2015**, *6* (11), 2032−2037.


https://doi.org/10.1021/jacs.1c11253
J. Am. Chem. Soc. 2022, 144, 3039−3049

(44) Liu, C.; Qian, J.; Ye, Y.; Zhou, H.; Sun, C. J.; Sheehan, C.; Zhang, Z.; Wan, G.; Liu, Y. S.; Guo, J.; Li, S.; Shin, H.; Hwang, S.; Gunnoe, T. B.; Goddard, W. A.; Zhang, S. Oxygen Evolution Reaction over Catalytic Single-Site Co in a Well-Defined Brookite $TiO_2$ Nanorod Surface. *Nat. Catal.* **2021**, *4* (1), 36−45.

(45) An, P.; Wei, L.; Li, H.; Yang, B.; Liu, K.; Fu, J.; Li, H.; Liu, H.; Hu, J.; Lu, Y.-R.; Pan, H.; Chan, T.-S.; Zhang, N.; Liu, M. Enhancing $CO_2$ Reduction by Suppressing Hydrogen Evolution with Polytetrafluoroethylene Protected Copper Nanoneedles. *J. Mater. Chem. A* **2020**, *8* (31), 15936−15941.

(46) Zhuang, T. T.; Pang, Y.; Liang, Z. Q.; Wang, Z.; Li, Y.; Tan, C. S.; Li, J.; Dinh, C. T.; De Luna, P.; Hsieh, P. L.; Burdyny, T.; Li, H. H.; Liu, M.; Wang, Y.; Li, F.; Proppe, A.; Johnston, A.; Nam, D. H.; Wu, Z. Y.; Zheng, Y. R.; Ip, A. H.; Tan, H.; Chen, L. J.; Yu, S. H.; Kelley, S. O.; Sinton, D.; Sargent, E. H. Copper Nanocavities Confine Intermediates for Efficient Electrosynthesis of $C_3$ Alcohol Fuels from Carbon Monoxide. *Nat. Catal.* **2018**, *1* (12), 946−951.

(47) Chen, K.; Liu, K.; An, P.; Li, H.; Lin, Y.; Hu, J.; Jia, C.; Fu, J.; Li, H.; Liu, H.; Lin, Z.; Li, W.; Li, J.; Lu, Y. R.; Chan, T. S.; Zhang, N.; Liu, M. Iron Phthalocyanine with Coordination Induced Electronic Localization to Boost Oxygen Reduction Reaction. *Nat. Commun.* **2020**, *11* (1), 1−8.

(48) Malkani, A. S.; Li, J.; Anibal, J.; Lu, Q.; Xu, B. Impact of Forced Convection on Spectroscopic Observations of the Electrochemical CO Reduction Reaction. *ACS Catal.* **2020**, *10* (2), 941−946.

(49) Wuttig, A.; Liu, C.; Peng, Q.; Yaguchi, M.; Hendon, C. H.; Motobayashi, K.; Ye, S.; Osawa, M.; Surendranath, Y. Tracking a Common Surface-Bound Intermediate during $CO_2$-to-Fuels Catalysis. *ACS Cent. Sci.* **2016**, *2* (8), 522−528.

(50) Katayama, Y.; Nattino, F.; Giordano, L.; Hwang, J.; Rao, R. R.; Andreussi, O.; Marzari, N.; Shao-Horn, Y. An in Situ Surface-Enhanced Infrared Absorption Spectroscopy Study of Electrochemical $CO_2$ Reduction: Selectivity Dependence on Surface C-Bound and O-Bound Reaction Intermediates. *J. Phys. Chem. C* **2019**, *123* (10), 5951−5963.

(51) Li, H.; Qin, X.; Jiang, T.; Ma, X.; Jiang, K.; Cai, W. Changing the Product Selectivity for Electrocatalysis of $CO_2$ Reduction Reaction on Plated Cu Electrodes. *ChemCatChem.* **2019**, *11* (24), 6139−6146.

(52) Heyes, J.; Dunwell, M.; Xu, B. $CO_2$ Reduction on Cu at Low Overpotentials with Surface-Enhanced in Situ Spectroscopy. *J. Phys. Chem. C* **2016**, *120* (31), 17334−17341.

(53) Borguet, E.; Dai, H. L. Site-Specific Properties and Dynamical Dipole Coupling of CO Molecules Adsorbed on a Vicinal Cu(100) Surface. *J. Chem. Phys.* **1994**, *101* (10), 9080−9095.

(54) Kresse, G.; Hafner, J. Ab Initio Molecular-Dynamics Simulation of the Liquid-Metal−Amorphous-Semiconductor Transition in Germanium. *Phys. Rev. B* **1994**, *49* (20), 14251−14269.

(55) Blöchl, P. E. Projector Augmented-Wave Method. *Phys. Rev. B* **1994**, *50* (24), 17953−17979.

(56) Perdew, J. P.; Burke, K.; Ernzerhof, M. Generalized Gradient Approximation Made Simple. *Phys. Rev. Lett.* **1996**, *77* (18), 3865−3868.

(57) Lee, S. Y.; Jung, H.; Kim, N.-K.; Oh, H.-S.; Min, B. K.; Hwang, Y. J. Mixed Copper States in Anodized Cu Electrocatalyst for Stable and Selective Ethylene Production from $CO_2$ Reduction. *J. Am. Chem. Soc.* **2018**, *140* (28), 8681−8689.

(58) Zhu, S.; Jiang, B.; Cai, W.-B.; Shao, M. Direct Observation on Reaction Intermediates and the Role of Bicarbonate Anions in $CO_2$ Electrochemical Reduction Reaction on Cu Surfaces. *J. Am. Chem. Soc.* **2017**, *139* (44), 15664−15667.

(59) Zhang, H.; Chang, X.; Chen, J. G.; Goddard, W. A.; Xu, B.; Cheng, M.-J.; Lu, Q. Computational and Experimental Demonstrations of One-Pot Tandem Catalysis for Electrochemical Carbon Dioxide Reduction to Methane. *Nat. Commun.* **2019**, *10* (1), 3340.





https://doi.org/10.1021/jacs.1c11253
*J. Am. Chem. Soc.* 2022, 144, 3039−3049